processes

MDPI

Article

Computational Fluid Dynamics, Transport, and Chemical Kinetics-Based Monolith Catalyst Dimensioning Methodology for Cost-Effective Performance

Jure Voglar [1,*], Andraž Pavlišič [1] and Blaž Likozar [1,2,3,4]

[1] Department of Catalysis and Chemical Reaction Engineering, National Institute of Chemistry, Hajdrihova 19, 1001 Ljubljana, Slovenia
[2] Faculty of Chemistry and Chemical Technology, University of Ljubljana, Večna pot 113, 1001 Ljubljana, Slovenia
[3] Faculty of Chemistry and Chemical Engineering, University of Maribor, Smetanova ulica 17, 2000 Maribor, Slovenia
[4] Faculty of Polymer Technology, Ozare 19, 2380 Slovenj Gradec, Slovenia
* Correspondence: jure.voglar@ki.si

Abstract: The newly developed computational fluid dynamics, transport, and chemical kinetics-based monolith catalyst dimensioning methodology consists of the following steps: (i) initial calculations, which generate some of the data, e.g., average inlet fluid velocity used in the (ii) computational fluid dynamics (CFD) modelling, which uses the laminar flow interface and the transport of diluted species interface while the user has to provide the kinetics of the reactions; (iii) the model order reduction uses a modified version of the plug flow reactor model and the linear pressure variation model; and (iv) the dimensioning optimization algorithm extracts the optimal monolith catalyst's channel geometry, which satisfies the user's performance constraints and reduces material consumption. Therefore, the methodology enables chemical engineers to quickly and efficiently design and dimension monolith catalysts for many different applications in an environmentally friendly way, which enables them to reduce both the material and operating costs while maintaining sufficient catalyst performance and, therefore, achieve its cost-effective performance.

Keywords: computational fluid dynamics; chemical kinetics; monolith catalyst; cost reduction; optimization

Citation: Voglar, J.; Pavlišič, A.; Likozar, B. Computational Fluid Dynamics, Transport, and Chemical Kinetics-Based Monolith Catalyst Dimensioning Methodology for Cost-Effective Performance. *Processes* **2024**, *12*, 1704. https://doi.org/10.3390/pr12081704

Academic Editor: Vladimir S. Arutyunov

Received: 8 July 2024
Revised: 12 August 2024
Accepted: 13 August 2024
Published: 14 August 2024

1. Introduction

The advantages of structured catalysts over fixed-bed reactors are their lower maldistribution and pressure drop [1], which is why they are widely used in chemical industry. The monolith catalysts have been in use in chemical engineering applications both for gas phase and gas–liquid reactions [2,3]. The gas phase reactions include (i) emission control of CO, unburned hydrocarbons (HC) and nitrogen oxides (NO_X) [4–6], (ii) catalytic combustion [7–9], (iii) steam reforming [10–12], (iv) methanation [13,14], (v) hydrogenation/dehydrogenation [15,16], (vi) oxidation [17–19], and (vii) water gas shift reaction [20,21]. Since many industrial processes depend on monolith catalysts, their optimized design, accurate modelling, effective performance, and reduced material toxicity are essential in multiple sectors of our society.

The computational fluid dynamics (CFD) modelling approach has been widely used to simulate processes of mass transfer and chemical kinetics inside monolith catalysts. Many studies have focused on either varying design/geometry [22–24] and/or predicting catalyst performance [25–27]. However, not many authors, e.g., [28], have used or combined their CFD results with one-dimensional (1D) monolith catalyst modelling. A one-dimensional modelling approach is often used for optimizing monolith design and configurations by manufactures [29]. Model order reduction (MOR) methodology could help monolith

designers by converting often computationally costly CFD modelling approach to simple 1D model calculations.

Multiple reduced order models for modelling of washcoated monolithic catalysts are presented in the available literature. However, most of the reduced order models are quite complex with multiple partial differential equations [30], transverse averaging using the Lyapunov–Schmidt method, look-up tables [31], and/or multiple matrices, e.g., the Thiele matrix [32]. Our approach, on the other hand, used only two simple algebraic equations to model the cross-sectional average (perpendicular to the flow direction) values of concentration and pressure (computed via CFD approach), respectively.

Some of the commonly used active catalyst materials are expensive, e.g., Pt [33], are toxic, e.g., V_2O_5 [34], are hard or impossible to recycle [35], and/or have no adequate alternative materials (e.g., Pt). Therefore, a reduction in the use of these crucial materials would reduce the manufacturing cost and the negative environmental impact of the monolith catalysts, considering their whole life cycle.

Chemical engineers who design and dimension a monolithic catalytic converter usually know the composition and the volumetric flow rate (Q) of their gas mixtures, the minimal required monolith catalyst performance (usually conversion of specific species or selectivity), maximal allowed pressure drop across the monolith channels, and the space constrains dedicated to the catalyst. Therefore, these elements are the input parameters for the developed dimensioning methodology. The chemical kinetics of the reactions occurring in the monolith catalyst should also be known in the form of rate law(s), as are, for example, for some selective catalytic reduction denitrification (SCR-deNO_X) catalysts which use ammonia as a reducing agent [24,36,37].

The usefulness of the CFD-based monolith catalyst dimensioning methodology was illustrated on a hypothetical case of an automotive SCR-deNO_X washcoated monolithic catalyst (WMC) for the removal of nitrogen oxides from flue gasses emitted by a personal vehicle with a hydrogen-powered internal combustion engine drivetrain.

2. Methods

The monolith catalyst dimensioning methodology consists of four main consecutive steps: (i) initial calculations, (ii) CFD modelling, (iii) model order reduction; and (iv) the dimensioning optimization algorithm.

2.1. Initial Calculations

The typical automotive cylindrical monoliths have diameters (D_m) of 100 mm and lengths (L_m) of 150 mm [38]. These dimensions were also considered in our example of designing and dimensioning of an automotive SCR-deNO_X catalyst. The share of effective flow area (Sh_{eff}) was assumed to be equal to 0.6 to account for the thickness of the monolith's walls which enable its structural integrity, load bearing capacity, and mechanical resistivity. The arrangement of the channels in the monolith catalyst was expected to follow the hexagonal-lattice-based circle packing pattern (of equally sized circles), which has been used in monoliths [39] and can be seen in Figure 1 [39]. The hexagonal-lattice-based circle packing is the densest circle packing in the plane with a packing density equal to $\frac{\pi}{2\sqrt{3}} \approx 0.9069$ [40]. This circle packing density is of course a theoretical limit, which, if applied to our case, would mean that the monolith's walls would have zero thickness and the monolith would have no extra material near its outer edges. Therefore, a considerably lower value than the 0.9069 theoretical limit was selected for the share of effective flow area (Sh_{eff}).

The average fluid velocity (u_{av}) flowing through the effective flow area (A_{eff}) was, therefore, determined using Equation (1).

$$u_{av} = \frac{Q}{A_{eff}} = \frac{Q}{Sh_{eff}\frac{\pi}{4}{D_m}^2} \quad (1)$$

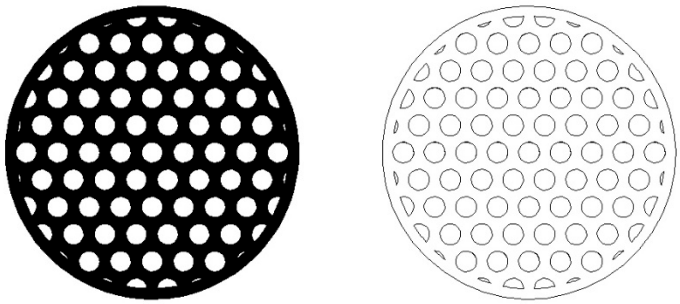

Figure 1. Cross-section (**left**) and drawing (**right**) of a cylindrical monolith with the hexagonal-lattice-based packing of cylindrical channels.

In case of the selected volumetric flow rate of 3.3×10^{-2} m^3/s, the average velocity is, in this case, equal to 7 m/s. This value of velocity was used as an input for the subsequent CFD studies.

The radii (R) of the individual cylindrical monolith channels were determined with Equation (2), where N is the number of monolith channels and varied from 600 to 6000 by steps of 50 (109 different radii, see Table A1).

$$R = \left| \sqrt{\frac{A_{eff}}{\pi N}} \right| \tag{2}$$

The channels' walls are assumed to be coated with a uniformly thick layer of high surface area washcoat that contains dispersed active catalyst material [41].

2.2. CFD Modelling

The CFD studies were conducted using the COMSOL Multiphysics® (version 5.1, COMSOL S.r.l., Brescia, Italy) simulation platform with two-dimensional (2D) axisymmetric stationary studies employing the laminar flow interface (spf, [42]) and the transport of diluted species interface (tds, [43]).

The Navier–Stokes equation of single-phase steady state incompressible laminar flow is Equation (3), where ρ denotes fluid density, u is the velocity, p is the pressure, I is the identity matrix, μ is the dynamic viscosity, and F represents the volume forces.

$$\rho(u \cdot \nabla)u = \nabla\left[-p\mathrm{I} + \mu\left(\nabla u + (\nabla u)^{\mathrm{T}}\right)\right] + F \tag{3}$$

Equation (4) is the continuity equation.

$$\rho \nabla u = 0 \tag{4}$$

The inflow at the inlet of a single cylindrical catalyst channel was selected to be the laminar inflow with a parabolic velocity profile. The working fluid was assumed to be produced during combustion of hydrogen with air and to enter the monolith channel at the temperature 300 °C, which is within the optimal operating temperature range of multiple commercial deNO$_X$ catalysts [44]. The fluid's density was determined with the ideal gas law and the calculation of the average gas mixture's molecular weight, while viscosity was determined with the method of Wilke [45]. For the combustion products of hydrogen (with air) at the equivalence ratio of 1.15 (see Table B.1 of Voglar et al. [46]) at 300 °C, the destiny equalled 0.5319 kg/m^3 and the dynamic viscosity was 2.597×10^{-5} Pa·s. In all of the studies, the average inlet fluid velocity was set to 7 m/s. The outlet had the pressure (0 Pa) boundary condition with suppressed backflow.

The transport of diluted species interface models the chemical species' transport through diffusion (Fick's second law) and convection. This Equation (5) is used, where D_i

denotes the diffusion coefficient of the species i, c_i is the concentration of the species i, and R_i is the reaction rate expression of the species i.

$$\nabla \cdot (-D_i \nabla c_i) + u \cdot \nabla c_i = R_i \quad (5)$$

The mass conservation equation for one or more chemical species i has a form of Equation (6), where N_i denotes the flux of the species i.

$$N_i = -D_i \nabla c_i + u c_i \quad (6)$$

The velocity field was inserted from the laminar flow interface (spf) calculations. Diffusion coefficients of both species A and B were set to 1×10^{-5} m^2/s, which is within the range typical for gaseous species [47].

The initial (inlet) concentration of species A, simulating species of nitrogen oxides (NO_X), was set to 1×10^{-2} mol/m^3, since the usual NO_X level is around 500 ppm [48,49], which equals to 1.06×10^{-2} mol/m^3 (at 300 °C). The inlet concentration of species B, representing the molecular nitrogen (N_2) and water vapour (H_2O) produced by the SCR-deNO_X reactions, was set to 0 mol/m^3.

This simple chemical reaction (Equation (7)) was assumed to take place at the fluid–cylinder wall interface (inside the monolith catalyst channel).

$$A \rightarrow B \quad (7)$$

The reaction was introduced as a flux boundary condition within the transport of diluted species interface (tds). Since the reaction is equimolar, it does not affect the flow regime by producing additional molecules and also simulates well the three main SCR-deNO_X reactions (standard, fast, and NO_2 SCR reaction), which have their molar ratio between products and reactants close to one (from 1.111 to 1.357).

The reaction rate (r) equation is this Equation (8).

$$r = k c_A \quad (8)$$

The reaction constant k has a unit of m/s because it models a surface reaction. The value of the reaction rate coefficient, k, was set to 1×10^6 m/s.

The inward fluxes of the species A and B (R_A and R_B) at the cylinder wall were determined with Equations (9) and (10).

$$R_A = -r \quad (9)$$

$$R_B = r \quad (10)$$

Our CFD studies modelled the external mass transfer effects while the internal mass transfer (through the pores of the catalyst material) was neglected. The reaction kinetics did not present the majority of the resistance, while the transport of species to the catalyst surface presented the main conversion limitation.

The computational domain's meshing was conducted with the selection of a physics-controlled mesh with a normal element size. Since our paper introduces a new catalyst dimensioning methodology and is not focused on generating accurate results, a grid independence study was, in our case, not performed. However, a grid independence study, verification, and experimental validation (on at least a couple of different monolith geometries) are advised to be carried out when our methodology is utilized in a real case of dimensioning of a monolith catalyst.

The temperature of the system was assumed to be constant 573.15 K (300 °C). The system was, therefore, adiabatic and isothermal, which is consistent with the other numerical studies, e.g., [50,51].

2.3. Model Order Reduction

When we extracted the relevant CFD data (pressure drop, concentrations of species), we continued our work with model order reduction (MOR) to simplify and enable our further methodological steps. The model order reduction methodology was applied to the CDF results. The model for determining the average concentration of species A inside the monolith channel varying with the monolith length (l) is the slightly modified version of the standard one-dimensional plug flow reactor (PFR) model (Equation (11)) [52], where $c_{A,in}$ is the inlet concentration of species A and k_c is the model constant, which describes the mass transport phenomena (by convection and diffusion) and reaction kinetics.

$$c_A = c_{A,in} e^{-k_c l} \tag{11}$$

The model for the pressure variation across the channel's length is well known to be linear [53], so Equation (12) was used, where p_{in} is the inlet pressure and k_p represents the model constant. We will name this model the linear pressure variation (LPV) model.

$$p = p_{in} - k_p l \tag{12}$$

The values of the model constants were extracted from the CFD results, where radially averaged values of the concentration of species A and pressure were sampled at the (equally spaced) nine lengths of the monolith channel. The model fitting was performed in the Python programming language (version 3.8.10) using the Spyder (version 5) integrated development environment (IDE).

2.4. Dimensioning Optimization Algorithm

The cost-effective monolith catalyst performance optimization algorithm was written in the Python programming language using the Spyder integrated development environment (IDE).

At this stage, the user has to provide the algorithm with two of the most relevant catalyst performance indicators: desired conversion (in our case 0.95 [54]) and maximal allowed pressure drop (in our case 560 Pa [55]).

The conversion of species A (Con_A) is defined in Equation (13), where $c_{A,in}$ and $c_{A,out}$ are the inlet and outlet concentrations of the species A, respectively.

$$Con_A = 1 - \frac{c_{A,out}}{c_{A,in}} \tag{13}$$

The algorithm firstly extracted all of the geometries with conversions equal or higher than the desired conversion. The leftover channels would have to be longer than the initial length limitation (150 mm) to satisfy the conversion criterium. Secondly, the algorithm used the PFR model to calculate the optimal channel lengths (L) with conversions equal to the desired conversion and applied the LPV model to determine the corresponding pressure drops (Δp). The next step was the elimination of the channels with too large pressure drops. Finally, the cost of the monolith catalyst was considered.

The cost of washcoated monolith catalyst manufacturing is correlated with the quantity of the active catalyst material used, since it usually contains expansive materials, e.g., precious metals [56]. The volume (V) of the used active catalyst material, which is uniformly coated in a thin layer (of thickness δ) on the inner surface of the individual cylindrical monolith channel, can be determined with Equation (14).

$$V = \pi\left((R+\delta)^2 - R^2\right)L = \pi\left(R^2 + 2R\delta + \delta^2 - R^2\right)L = \pi\left(2R\delta + \delta^2\right)L \tag{14}$$

In cases of thin coatings ($\delta << R$), the volume of the active catalyst material for an individual catalyst channel can be estimated using Equation (15).

$$V \cong (2\pi R)\delta L \tag{15}$$

Since the coating thickness (δ) is assumed to be constant for a specific type of an active catalyst material, the cost of the coating material for an individual catalyst channel is proportional to the product of the radius (R) and length (L) of the cylindrical monolith channel. Because the monolith catalyst has multiple (N) parallel cylindrical channels coated with an active catalyst material, the cost of the monolith catalyst ($Cost$) can be estimated with Equation (16).

$$Cost \propto NRL \tag{16}$$

The last step of the algorithm involves the optimization of the cost-effectiveness of the monolith catalyst. After calculating the estimated cost for the active catalyst material, the algorithm finds the case with the minimal cost from the already sifted geometries with adequate performance both in terms of conversion and pressure drop. Therefore, the algorithm enables chemical engineers to find the cost-effectiveness-optimized monolith catalyst geometry which satisfies their performance and space constraint criteria.

3. Results and Discussion

The initial assumptions of our hypothetical case, along with the results of the initial calculations, are already presented in Section 2. The main aim of the initial calculations was to extract the relevant data to be used as the boundary conditions of the following CFD studies.

The CFD studies were performed on the geometries of cylindrical monolith channels with lengths of 150 mm and 109 different radii (R) varying from 0.50 mm up to 1.58 mm. The Reynolds numbers (Re) of our CFD studies varied between 143 and 453 (see Table A1).

The velocity field was, as expected, unchanging with the axial direction of the channel, since the inlet velocity profile inserted as the boundary condition was already parabolic—a fully developed laminar flow (Figure 2a). The pressure inside the monolith channels monotonically decreased with increasing channel length, while it had close to zero variation in the radial direction (Figure 2b). This type of spatial pressure variation is typical for laminar flow inside a channel.

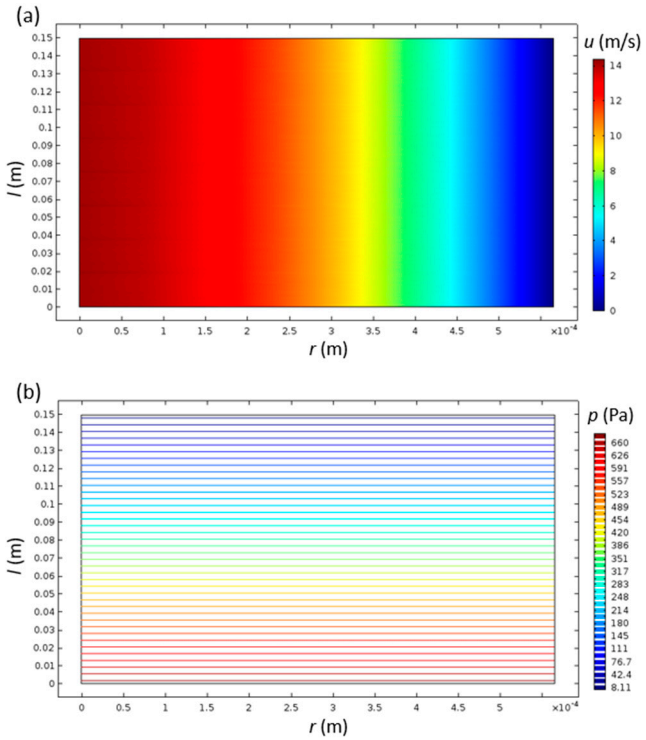

Figure 2. Velocity (**a**) and pressure (**b**) distributions inside the cylindrical monolith catalyst channel with R = 0.565 and L = 150 mm.

The concentrations of species A and B have high gradients near the inlet, while they settle to a more uniform distribution at the outlet (Figure 3). Since both of the diffusion coefficients are the same, the contours of both of the species are inverse to each other, as expected.

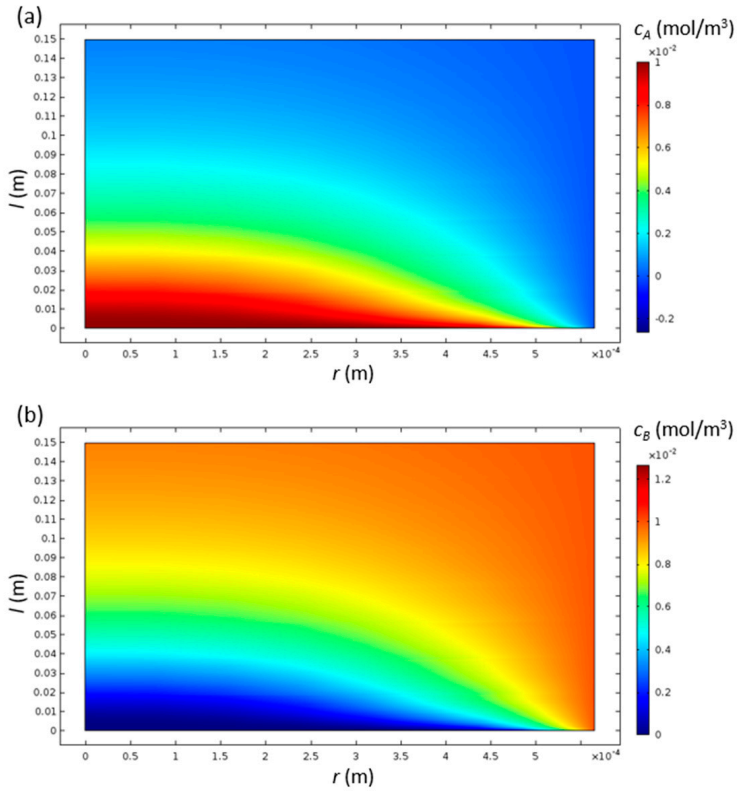

Figure 3. Contours of concentrations of species A (**a**) and B (**b**) inside the cylindrical monolith catalyst channel with R = 0.565 and L = 150 mm.

The conversions of species A varied from 0.4540 (at R = 1.581) to 0.9812 (at R = 0.500), while the pressure drops varied from 88 Pa (at R = 1.581) to 874 Pa (at R = 0.500). Small diameter channels exhibited high conversion accompanied with high pressure drop, and large diameter channels had low conversion with low pressure drop. Therefore, the trade-off between a high conversion and a high pressure drop is clearly present (Table A1), so the engineers have to be aware of it and consider it during the design and dimensioning of the monolith catalysts.

The model order reduction results are also presented in Table A1. The values of the coefficients k_c and k_p both monotonically decrease as the channel radius increases. The coefficient of determination (R^2) values for the PFR model varied from 0.881 to 0.995, and for the LPV model from 0.999997 to 1.0. The R^2 values monotonically decreased as the channel radius increased, which could be explained for the PFR model by an increase in departure from the PFR model's assumptions by an increase in the radial gradients of velocity and species concentrations. Since the algorithm firstly eliminated the geometries with insufficient conversion (with index values from 36 to 109), the MOR models with the smallest values of R^2 used in further calculations of optimal channel lengths were 0.991 and 1.0 for the PFR and the LPV models, respectively.

An example of model order reduction fits to radially averaged concentration of species A and pressure is presented in Figure 4.

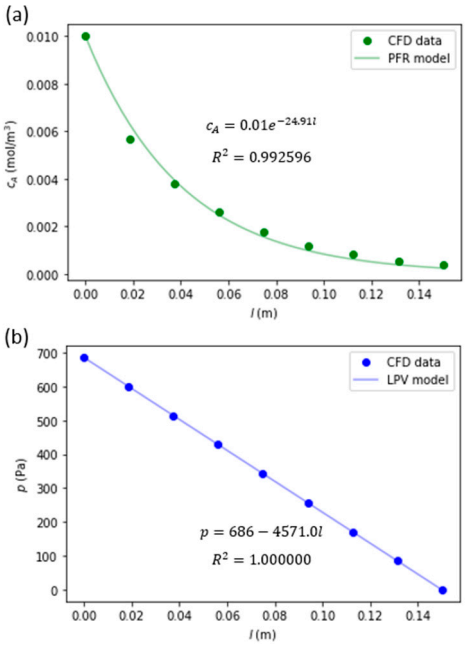

Figure 4. Model order reduction fitting results of c_A (**a**) and p (**b**) for the cylindrical monolith catalyst channel with R = 0.565 and L = 150 mm.

Table 1 contains the channel geometries which enable sufficient conversion of 0.95, and are optimized in length based on the calculated parameters of the PRF model in the MOR stage of the method. The length optimization reduced both the cost and the pressure drops by up to 34.4%, since both the used monolith material volume and the pressure drop are linearly dependent on the channel's length, originating from Equation (15) and the LPV model, respectively.

Table 1. The list of the monolith catalysts' dimensional characteristics, calculated pressure drops, and lengths for achievement of the target conversion of 0.95 with accompanied cost reductions (*CR*).

Index (/)	*R* (mm)	*N* (/)	Δ*p* (Pa)	*L* (mm)	*CR* (%)
1	0.500	6000	573	98.4	34.4
2	0.502	5950	574	99.2	33.8
3	0.504	5900	572	99.8	33.4
4	0.506	5850	576	101.3	32.4
5	0.509	5800	571	101.4	32.4
6	0.511	5750	573	102.5	31.6
7	0.513	5700	571	103.1	31.3
8	0.515	5650	571	104.1	30.6
9	0.518	5600	567	104.1	30.6
10	0.520	5550	567	105.1	29.9
11	0.522	5500	568	106.2	29.2
12	0.525	5450	569	107.4	28.4
13	0.527	5400	569	108.4	27.8
14	0.530	5350	568	109.3	27.1
15	0.532	5300	568	110.3	26.5
16	0.535	5250	570	111.6	25.6
17	0.537	5200	566	112.1	25.3
18	0.540	5150	568	113.5	24.3
19	0.542	5100	565	114.0	24.0
20	0.545	5050	568	115.7	22.9

Table 1. *Cont.*

Index (/)	*R* (mm)	*N* (/)	Δ*p* (Pa)	*L* (mm)	*CR* (%)
21	0.548	5000	567	116.7	22.2
22	0.550	4950	564	117.2	21.9
23	0.553	4900	564	118.3	21.1
24	0.556	4850	563	119.4	20.4
25	0.559	4800	561	120.2	19.9
26	0.562	4750	563	122.0	18.7
27	**0.565**	**4700**	**550**	**120.3**	**19.8**
28	0.568	4650	549	121.4	19.1
29	0.571	4600	546	122.0	18.7
30	0.574	4550	546	123.3	17.8
31	0.577	4500	545	124.4	17.1
32	0.581	4450	547	126.3	15.8
33	0.584	4400	546	127.5	15.0
34	0.587	4350	548	129.4	13.7
35	0.591	4300	548	131.1	12.6

The bold values relate to the optimal monolith catalyst geometry.

After consideration of the maximal allowed pressure drop of 560 Pa, the number of viable geometries reduces to 9 (Table 2). The optimal geometry among the list was selected based on the material cost estimated with Equation (16). The optimal monolith catalyst geometry was the one with index number 27, which had 4700 parallel cylindrical channels with radii of 0.565 mm and lengths of 120.3 mm. Compared to the viable monolith geometry with the highest estimated material cost (index 35), the optimal geometry reduced the material cost by 4.1%.

Table 2. The list of the monolith catalysts' dimensional characteristics, calculated pressure drops, lengths, and estimated material cost for achievement of the target conversion of 0.95 and pressure drop below the set limit of 560 Pa with accompanied cost reductions.

Index (/)	*R* (mm)	*N* (/)	Δ*p* (Pa)	*L* (mm)	*Cost* (/)	*CR* (%)
27	**0.565**	**4700**	**550**	**120.3**	**0.3194**	**4.1**
28	0.568	4650	549	121.4	0.3206	3.7
29	0.571	4600	546	122.0	0.3205	3.7
30	0.574	4550	546	123.3	0.3221	3.2
31	0.577	4500	545	124.4	0.3232	2.9
32	0.581	4450	547	126.3	0.3263	2.0
33	0.584	4400	546	127.5	0.3276	1.6
34	0.587	4350	548	129.4	0.3306	0.7
35	0.591	4300	548	131.1	0.3329	0.0

The bold values relate to the optimal monolith catalyst geometry.

If we retrace the optimal monolith geometry with index number 27, we can observe from Table 1 that shortening the length from the initial 150 mm reduced its material cost and pressure drop by 19.8%. The total cost reduction enabled by our monolith dimensioning methodology is hard to predict in real conditions and is dependent on the many factors (e.g., initial/reference catalyst design and geometry) and specific characteristics of the case.

Our estimation is that our methodology would enable chemical engineers to save precious catalyst material of up to 20% and at the same time reduce the operating costs of monolith catalysts via a reduced pressure drop.

4. Conclusions

The presented MOR model was able to successfully reduce the order of the modelling approach with sufficient accuracy and therefore is suitable for modelling small diameter (<2 mm) cylindrical channels, typically used in monolith catalysts. The two-dimensional

CFD modelling results from a single cylindrical monolith channel are described using two simple algebraic equations. The first one deals with cross-sectional average of concentration (of species A; modified PFR model) with R^2 values ranging from 0.881 to 0.995. The second one (LPV model) models the pressure evolution across the channel's length, with accuracy related to R^2 values equal to or above 0.999997.

Our approach includes the assessment of the washcoat monolith's material cost with a simple method for assessing the consumption of an active catalyst material which coats the catalyst's support in a relatively thin (compared to the channel's dimensions) and uniform manner. The calculated cost of the active catalyst material served us in the selection process within the dimensioning optimization algorithm.

The newly developed computational fluid dynamics, transport, and chemical kinetics-based monolith catalyst dimensioning methodology enables chemical engineers to design and dimension monolith catalysts for many different applications in silico, which enable them to reduce both the material and operation costs while maintaining sufficient catalyst performance and, therefore, achieve its cost-effective performance. According to our results and estimations, the material savings could be in the range of up to 20%.

The presented monolith catalyst dimensioning methodology was conducted in a case of a washcoated monolith catalyst (WMC). However, it could easily be adapted to dimensioning a bulk monolithic catalyst (BMC) with alterations to the estimated material cost equation (Equation (16)).

Our methodology is relatively simple and easy to implement since the user has to know just a few basic initial conditions like space constrains, inflow conditions, the range in the number of catalyst channels, and performance targets, e.g., conversion and pressure drop. From there forward, the only real requirement is having a working computer with sufficient performance characteristics (e.g., computational power, random-access memory (RAM) size), and installed CFD software and some other data processing software which enables the user to virtually test an array of multiple possible monolith catalyst designs and geometries to extract the optimal one for the designated purpose. Therefore, the developed methodology not only reduces the material and operation costs, as already mentioned, but also saves engineers the substantial amount of time and effort required to experimentally test multiple potential catalyst geometries, since only the tests required for validation of the CFD calculations and the tests of the monolith catalyst prototype are necessary.

Author Contributions: Conceptualization, J.V. and A.P.; methodology, J.V. and A.P.; software, J.V.; formal analysis, J.V. and A.P.; investigation, J.V.; data curation, J.V.; writing—original draft, J.V.; writing—review & editing, J.V., A.P. and B.L.; visualization, J.V.; supervision, B.L.; project administration, B.L.; funding acquisition, B.L. All authors have read and agreed to the published version of the manuscript.

Funding: The work was funded by the Slovenian Research and Innovation Agency through core funding P2-0152 and project funding J7-4638.

Data Availability Statement: Data will be available on a reasonable request.

Conflicts of Interest: The authors declare no conflict of interest.

Appendix A. CFD Results and MOR Data Summary

Table A1. All of the considered monolith catalysts with initial length of 150 mm, their integral dimensional and performance characteristics, Reynolds numbers, and MOR model parameters with corresponding coefficients of determination (R^2).

Index (/)	R (mm)	N (/)	Δp (Pa)	Con_A (/)	Re (/)	k_c (1/m)	R^2 (/)	k_p (Pa/m)	R^2 (/)
1	0.500	6000	874	0.9812	143	30.45	0.995052	5829.2	1.000000
2	0.502	5950	867	0.9810	144	30.19	0.995086	5780.2	1.000000
3	0.504	5900	860	0.9801	145	30.00	0.995251	5732.7	1.000000

Table A1. *Cont.*

Index (/)	*R* (mm)	*N* (/)	Δ*p* (Pa)	Con_A (/)	*Re* (/)	k_c (1/m)	R^2 (/)	k_p (Pa/m)	R^2 (/)
4	0.506	5850	852	0.9793	145	29.56	0.994750	5683.9	1.000000
5	0.509	5800	845	0.9793	146	29.55	0.994571	5635.2	1.000000
6	0.511	5750	838	0.9786	146	29.22	0.994666	5586.6	1.000000
7	0.513	5700	831	0.9776	147	29.06	0.994395	5539.0	1.000000
8	0.515	5650	824	0.9774	148	28.79	0.994704	5490.8	1.000000
9	0.518	5600	816	0.9772	148	28.77	0.994608	5443.5	1.000000
10	0.520	5550	809	0.9764	149	28.50	0.994424	5394.4	1.000000
11	0.522	5500	802	0.9753	150	28.21	0.994275	5345.4	1.000000
12	0.525	5450	794	0.9743	150	27.89	0.994155	5297.1	1.000000
13	0.527	5400	787	0.9737	151	27.64	0.994292	5248.7	1.000000
14	0.530	5350	780	0.9724	152	27.41	0.993711	5199.0	1.000000
15	0.532	5300	773	0.9716	153	27.16	0.993869	5151.5	1.000000
16	0.535	5250	765	0.9704	153	26.84	0.993438	5102.4	1.000000
17	0.537	5200	758	0.9700	154	26.73	0.993488	5053.8	1.000000
18	0.540	5150	751	0.9690	155	26.39	0.993145	5006.0	1.000000
19	0.542	5100	743	0.9682	156	26.28	0.993280	4957.4	1.000000
20	0.545	5050	736	0.9669	156	25.90	0.993056	4908.4	1.000000
21	0.548	5000	729	0.9660	157	25.68	0.992873	4860.0	1.000000
22	0.550	4950	722	0.9654	158	25.56	0.992800	4812.1	1.000000
23	0.553	4900	715	0.9644	159	25.32	0.992759	4764.0	1.000000
24	0.556	4850	707	0.9631	160	25.09	0.992401	4714.6	1.000000
25	0.559	4800	700	0.9626	160	24.93	0.992461	4666.9	1.000000
26	0.562	4750	693	0.9610	161	24.56	0.991998	4618.3	1.000000
27	**0.565**	**4700**	**686**	**0.9622**	**162**	**24.91**	**0.992596**	**4571.0**	**1.000000**
28	0.568	4650	678	0.9612	163	24.68	0.992391	4523.2	1.000000
29	0.571	4600	671	0.9604	164	24.55	0.992352	4475.5	1.000000
30	0.574	4550	664	0.9596	165	24.30	0.992217	4426.9	1.000000
31	0.577	4500	657	0.9583	166	24.08	0.992139	4378.2	1.000000
32	0.581	4450	649	0.9563	167	23.72	0.991320	4329.4	1.000000
33	0.584	4400	642	0.9550	167	23.49	0.991487	4280.6	1.000000
34	0.587	4350	635	0.9524	168	23.15	0.991095	4232.2	1.000000
35	0.591	4300	627	0.9513	169	22.86	0.990751	4183.1	1.000000
36	0.594	4250	620	0.9495	170	22.72	0.990327	4133.9	1.000000
37	0.598	4200	613	0.9472	171	22.30	0.989910	4084.7	1.000000
38	0.601	4150	605	0.9454	172	22.04	0.989998	4036.0	1.000000
39	0.605	4100	598	0.9438	173	21.87	0.989740	3987.0	1.000000
40	0.609	4050	591	0.9411	175	21.49	0.989604	3938.0	1.000000
41	0.612	4000	583	0.9374	176	20.96	0.989082	3888.7	1.000000
42	0.616	3950	576	0.9341	177	20.62	0.988426	3839.5	1.000000
43	0.620	3900	568	0.9303	178	20.24	0.987491	3790.2	1.000000
44	0.624	3850	561	0.9279	179	19.93	0.987649	3741.2	1.000000
45	0.628	3800	554	0.9245	180	19.59	0.987004	3691.9	1.000000
46	0.632	3750	546	0.9223	181	19.37	0.986508	3643.1	1.000000
47	0.637	3700	539	0.9205	183	19.15	0.986923	3595.3	1.000000
48	0.641	3650	532	0.9178	184	18.94	0.986445	3546.3	1.000000
49	0.645	3600	525	0.9155	185	18.71	0.986071	3497.8	0.999999
50	0.650	3550	517	0.9126	186	18.44	0.985406	3449.2	0.999999
51	0.655	3500	510	0.9100	188	18.21	0.985677	3400.8	0.999999
52	0.659	3450	503	0.9072	189	17.96	0.984682	3352.3	0.999999
53	0.664	3400	496	0.9048	190	17.79	0.984604	3304.4	1.000000
54	0.669	3350	488	0.9025	192	17.58	0.984443	3255.7	0.999999
55	0.674	3300	481	0.9002	193	17.40	0.984127	3207.8	0.999999
56	0.679	3250	474	0.8975	195	17.19	0.983736	3159.5	0.999999
57	0.685	3200	467	0.8938	196	16.93	0.983234	3110.9	0.999999
58	0.690	3150	459	0.8924	198	16.86	0.983105	3062.5	0.999999
59	0.696	3100	452	0.8877	200	16.51	0.982191	3013.9	0.999999
60	0.701	3050	445	0.8867	201	16.43	0.982221	2966.3	0.999999

Table A1. *Cont.*

Index (/)	*R* (mm)	*N* (/)	Δ*p* (Pa)	Con_A (/)	*Re* (/)	k_c (1/m)	R^2 (/)	k_p (Pa/m)	R^2 (/)
61	0.707	3000	438	0.8839	203	16.25	0.982359	2917.7	0.999999
62	0.713	2950	430	0.8817	205	16.10	0.982212	2869.0	0.999999
63	0.719	2900	423	0.8779	206	15.85	0.981770	2820.5	0.999999
64	0.725	2850	416	0.8735	208	15.61	0.980241	2772.4	1.000000
65	0.732	2800	409	0.8699	210	15.36	0.980929	2724.0	0.999999
66	0.739	2750	401	0.8657	212	15.12	0.980276	2675.0	0.999999
67	0.745	2700	394	0.8571	214	14.69	0.978628	2625.7	0.999999
68	0.752	2650	387	0.8510	216	14.33	0.977858	2577.2	1.000000
69	0.760	2600	379	0.8451	218	14.08	0.977024	2528.3	0.999999
70	0.767	2550	372	0.8385	220	13.75	0.975798	2479.5	0.999999
71	0.775	2500	365	0.8335	222	13.53	0.974831	2430.5	0.999999
72	0.782	2450	357	0.8269	224	13.25	0.973394	2381.7	0.999999
73	0.791	2400	350	0.8208	227	13.05	0.971437	2333.0	0.999999
74	0.799	2350	343	0.8157	229	12.81	0.971131	2284.5	0.999999
75	0.808	2300	335	0.8087	232	12.51	0.970381	2235.8	0.999999
76	0.816	2250	328	0.8049	234	12.40	0.969208	2187.7	0.999999
77	0.826	2200	321	0.8007	237	12.21	0.968941	2139.1	0.999999
78	0.835	2150	314	0.7953	240	12.00	0.968407	2090.7	0.999999
79	0.845	2100	306	0.7879	242	11.76	0.966999	2042.4	0.999999
80	0.855	2050	299	0.7808	245	11.51	0.965259	1993.6	0.999999
81	0.866	2000	292	0.7752	248	11.31	0.964688	1945.2	0.999999
82	0.877	1950	285	0.7711	252	11.17	0.964817	1897.3	0.999999
83	0.889	1900	277	0.7634	255	10.93	0.962795	1848.8	0.999999
84	0.900	1850	270	0.7580	258	10.76	0.962640	1800.3	0.999999
85	0.913	1800	263	0.7501	262	10.51	0.961581	1751.9	0.999999
86	0.926	1750	255	0.7418	266	10.27	0.959729	1703.3	0.999999
87	0.939	1700	248	0.7319	269	9.99	0.957383	1653.9	0.999999
88	0.953	1650	241	0.7226	273	9.76	0.955118	1605.0	0.999999
89	0.968	1600	233	0.7067	278	9.33	0.951942	1555.5	0.999999
90	0.984	1550	226	0.6929	282	8.97	0.948455	1506.5	0.999999
91	1.000	1500	219	0.6860	287	8.83	0.947314	1458.2	0.999999
92	1.017	1450	211	0.6813	292	8.74	0.945683	1410.2	0.999999
93	1.035	1400	204	0.6692	297	8.45	0.944485	1361.6	0.999998
94	1.054	1350	197	0.6626	302	8.28	0.943402	1313.4	0.999998
95	1.074	1300	190	0.6525	308	8.07	0.941091	1264.9	0.999998
96	1.095	1250	182	0.6434	314	7.89	0.939183	1216.4	0.999998
97	1.118	1200	175	0.6324	321	7.67	0.937808	1167.3	0.999998
98	1.142	1150	168	0.6167	328	7.35	0.932660	1118.6	0.999998
99	1.168	1100	160	0.5970	335	6.99	0.925107	1069.3	0.999998
100	1.195	1050	153	0.5843	343	6.75	0.922493	1020.7	0.999998
101	1.225	1000	146	0.5735	351	6.56	0.919182	972.5	0.999998
102	1.257	950	139	0.5609	360	6.35	0.914481	923.9	0.999998
103	1.291	900	131	0.5490	370	6.15	0.912582	875.5	0.999998
104	1.328	850	124	0.5355	381	5.92	0.909780	826.9	0.999998
105	1.369	800	117	0.5161	393	5.62	0.901627	777.7	0.999997
106	1.414	750	109	0.4981	406	5.35	0.893601	728.8	0.999997
107	1.464	700	102	0.4856	420	5.16	0.890363	680.4	0.999997
108	1.519	650	95	0.4707	436	4.94	0.888446	632.1	0.999997
109	1.581	600	88	0.4540	453	4.70	0.880629	583.6	0.999997

The bold values relate to the optimal monolith catalyst geometry.

References

1. Cybulski, A.; Moulijn, J.A. Monoliths in Heterogeneous Catalysis. *Catal. Rev.—Sci. Eng.* **1994**, *36*, 179–270. [CrossRef]
2. Roy, S.; Bauer, T.; Al-Dahhan, M.; Lehner, P.; Turek, T. Monoliths as Multiphase Reactors: A Review. *AIChE J.* **2004**, *50*, 2918–2938. [CrossRef]
3. Boger, T.; Heibel, A.K.; Sorensen, C.M. Monolithic Catalysts for the Chemical Industry. *Ind. Eng. Chem. Res.* **2004**, *43*, 4602–4611. [CrossRef]

4. Gokalp, B. Using the Three-Way Catalyst Monolith Reactor for Reducing Exhaust Emissions. *J. Renew. Sustain. Energy* **2012**, *4*, 43114. [CrossRef]
5. Nandi, S.; Arango, P.; Chaillou, C.; Dujardin, C.; Granger, P.; Laigle, E.; Nicolle, A.; Norsic, C.; Richard, M. Relationship between Design Strategies of Commercial Three-Way Monolithic Catalysts and Their Performances in Realistic Conditions. *Catal. Today* **2022**, *384*, 122–132. [CrossRef]
6. Rico-Pérez, V.; García-Cortés, J.M.; De Lecea, C.S.-M.; Bueno-López, A. NOx Reduction to N_2 with Commercial Fuel in a Real Diesel Engine Exhaust Using a Dual Bed of Pt/Beta Zeolite and RhOx/Ceria Monolith Catalysts. *Chem. Eng. Sci.* **2013**, *104*, 557–564. [CrossRef]
7. Dupont, V.; Moallemi, F.; Williams, A.; Zhang, S. Combustion of Methane in Catalytic Honeycomb Monolith Burners. *Int. J. Energy Res.* **2000**, *24*, 1181–1201. [CrossRef]
8. Tacchino, S.; Vella, L.D.; Specchia, S. Catalytic Combustion of CH_4 and H_2 into Micro-Monoliths. *Catal. Today* **2010**, *157*, 440–445. [CrossRef]
9. Chao, Y.-C.; Chen, G.-B.; Hsu, H.-W.; Hsu, J.-R. Catalytic Combustion of Gasified Biomass in a Platinum Monolith Honeycomb Reactor. *Appl. Catal. A Gen.* **2004**, *261*, 99–107. [CrossRef]
10. Wu, P.; Li, X.; Ji, S.; Lang, B.; Habimana, F.; Li, C. Steam Reforming of Methane to Hydrogen over Ni-Based Metal Monolith Catalysts. *Catal. Today* **2009**, *146*, 82–86. [CrossRef]
11. Roh, H.-S.; Lee, D.K.; Koo, K.Y.; Jung, U.H.; Yoon, W.L. Natural Gas Steam Reforming for Hydrogen Production over Metal Monolith Catalyst with Efficient Heat-Transfer. *Int. J. Hydrogen Energy* **2010**, *35*, 1613–1619. [CrossRef]
12. Moraes, T.S.; Borges, L.E.P.; Farrauto, R.; Noronha, F.B. Steam Reforming of Ethanol on $Rh/SiCeO_2$ Washcoated Monolith Catalyst: Stable Catalyst Performance. *Int. J. Hydrogen Energy* **2018**, *43*, 115–126. [CrossRef]
13. Bustinza, A.; Frías, M.; Liu, Y.; García-Bordejé, E. Mono-and Bimetallic Metal Catalysts Based on Ni and Ru Supported on Alumina-Coated Monoliths for CO_2 Methanation. *Catal. Sci. Technol.* **2020**, *10*, 4061–4071. [CrossRef]
14. García-Moncada, N.; Navarro, J.C.; Odriozola, J.A.; Lefferts, L.; Faria, J.A. Enhanced Catalytic Activity and Stability of Nanoshaped Ni/CeO_2 for CO_2 Methanation in Micro-Monoliths. *Catal. Today* **2022**, *383*, 205–215. [CrossRef]
15. El Sawi, M.; Frusteri, F.; Parmaliana, A.; Formisano, B.; Giordano, N. A Kinetic Study of Cyclohexane Dehydrogenation on Pt Monolithic Catalyst. *J. Chem. Technol. Biotechnol.* **1986**, *36*, 122–128. [CrossRef]
16. Parmaliana, A.; Crisafulli, C.; Maggiore, R.; Bart, J.C.J.; Giordano, N. Catalytic Activity of Honeycomb Catalysts, I. The Benzene-Cyclohexane (de) Hydrogenation Reaction. *React. Kinet. Catal. Lett.* **1981**, *18*, 295–299. [CrossRef]
17. Tronconi, E.; Cavanna, A.; Orsenigo, C.; Forzatti, P. Transient Kinetics of SO_2 Oxidation over SCR-DeNO X Monolith Catalysts. *Ind. Eng. Chem. Res.* **1999**, *38*, 2593–2598. [CrossRef]
18. Subbanna, P.; Greene, H.; Desai, F. Catalytic Oxidation of Polychlorinated Biphenyls in a Monolithic Reactor System. *Environ. Sci. Technol.* **1988**, *22*, 557–561. [CrossRef]
19. Michael, B.C.; Nare, D.N.; Schmidt, L.D. Catalytic Partial Oxidation of Ethane to Ethylene and Syngas over Rh and Pt Coated Monoliths: Spatial Profiles of Temperature and Composition. *Chem. Eng. Sci.* **2010**, *65*, 3893–3902. [CrossRef]
20. Portela, R.; Wolf, P.; Marinkovic, J.M.; Serrano-Lotina, A.; Riisager, A.; Haumann, M. Tailored Monolith Supports for Improved Ultra-Low Temperature Water-Gas Shift Reaction. *React. Chem. Eng.* **2021**, *6*, 2114–2124. [CrossRef]
21. Quiney, A.S.; Germani, G.; Schuurman, Y. Optimization of a Water–Gas Shift Reactor over a Pt/Ceria/Alumina Monolith. *J. Power Sources* **2006**, *160*, 1163–1169. [CrossRef]
22. Liu, H.; Zhao, J.; Li, C.; Ji, S. Conceptual Design and CFD Simulation of a Novel Metal-Based Monolith Reactor with Enhanced Mass Transfer. *Catal. Today* **2005**, *105*, 401–406. [CrossRef]
23. Di Benedetto, A.; Di Sarli, V. CFD Modeling and Simulation of a Catalytic Micro-Monolith. *Int. J. Chem. React. Eng.* **2011**, *9*, e2526. [CrossRef]
24. Shin, S.B.; Skau, K.I.; Menon, M.; Maroor, S.; Spatenka, S. A Modelling Approach to Kinetics Study and Novel Monolith Channel Design for Selective Catalytic Reduction (SCR) Applications. *Chem. Eng. Res. Des.* **2019**, *142*, 412–428. [CrossRef]
25. Shaikh, S.K.; Pathan, K.A.; Chaudhary, Z.I.; Khan, S.A. CFD Analysis of an Automobile Catalytic Converter to Obtain Flow Uniformity and to Minimize Pressure Drop across the Monolith. *CFD Lett.* **2020**, *12*, 116–128. [CrossRef]
26. Sandu, V.-C.; Cormos, A.-M.; Dumbrava, I.-D.; Imre-Lucaci, A.; Cormos, C.-C.; de Boer, R.; Boon, J.; Sluijter, S. Assessment of CO_2 Capture Efficiency in Packed Bed versus 3D-Printed Monolith Reactors for SEWGS Using CFD Modeling. *Int. J. Greenh. Gas Control* **2021**, *111*, 103447. [CrossRef]
27. Sadeghi, F.; Tirandazi, B.; Khalili-Garakani, A.; Nasseri, S.; Nodehi, R.N.; Mostoufi, N. Investigating the Effect of Channel Geometry on Selective Catalytic Reduction of NOx in Monolith Reactors. *Chem. Eng. Res. Des.* **2017**, *118*, 21–30. [CrossRef]
28. Štěpánek, J.; Kočí, P.; Marek, M.; Kubíček, M. Catalyst Simulations Based on Coupling of 3D CFD Tool with Effective 1D Channel Models. *Catal. Today* **2012**, *188*, 87–93. [CrossRef]
29. Chen, J.; Yang, H.; Wang, N.; Ring, Z.; Dabros, T. Mathematical Modeling of Monolith Catalysts and Reactors for Gas Phase Reactions. *Appl. Catal. A Gen.* **2008**, *345*, 1–11. [CrossRef]
30. Ratnakar, R.R.; Bhattacharya, M.; Balakotaiah, V. Reduced Order Models for Describing Dispersion and Reaction in Monoliths. *Chem. Eng. Sci.* **2012**, *83*, 77–92. [CrossRef]
31. Nien, T.; Mmbaga, J.P.; Hayes, R.E.; Votsmeier, M. Hierarchical Multi-Scale Model Reduction in the Simulation of Catalytic Converters. *Chem. Eng. Sci.* **2013**, *93*, 362–375. [CrossRef]

32. Tu, M.; Ratnakar, R.; Balakotaiah, V. Reduced Order Models with Local Property Dependent Transfer Coefficients for Real Time Simulations of Monolith Reactors. *Chem. Eng. J.* **2020**, *383*, 123074. [CrossRef]
33. Pérez-Cadenas, A.F.; Kapteijn, F.; Moulijn, J.A.; Maldonado-Hódar, F.J.; Carrasco-Marín, F.; Moreno-Castilla, C. Pd and Pt Catalysts Supported on Carbon-Coated Monoliths for Low-Temperature Combustion of Xylenes. *Carbon* **2006**, *44*, 2463–2468. [CrossRef]
34. Consentino, L.; Pantaleo, G.; Parola, V.L.; Migliore, C.; Greca, E.L.; Liotta, L.F. NH_3-NO SCR Catalysts for Engine Exhaust Gases Abatement: Replacement of Toxic V_2O_5 with MnOx to Improve the Environmental Sustainability. *Top. Catal.* **2023**, *66*, 850–859. [CrossRef]
35. Ferella, F. A Review on Management and Recycling of Spent Selective Catalytic Reduction Catalysts. *J. Clean. Prod.* **2020**, *246*, 118990. [CrossRef]
36. Metkar, P.S.; Harold, M.P.; Balakotaiah, V. Experimental and Kinetic Modeling Study of NH3-SCR of NOx on Fe-ZSM-5, Cu-Chabazite and Combined Fe- and Cu-Zeolite Monolithic Catalysts. *Chem. Eng. Sci.* **2013**, *87*, 51–66. [CrossRef]
37. Colombo, M.; Nova, I.; Tronconi, E. Detailed Kinetic Modeling of the NH3–NO/NO_2 SCR Reactions over a Commercial Cu-Zeolite Catalyst for Diesel Exhausts after Treatment. *Catal. Today* **2012**, *197*, 243–255. [CrossRef]
38. Benjamin, S.F.; Liu, Z.; Roberts, C.A. Automotive Catalyst Design for Uniform Conversion Efficiency. *Appl. Math. Model.* **2004**, *28*, 559–572. [CrossRef]
39. Baharudin, L.; Watson, M.J. Monolithic Substrate Support Catalyst Design Considerations for Steam Methane Reforming Operation. *Rev. Chem. Eng.* **2018**, *34*, 481–501. [CrossRef]
40. Chang, H.-C.; Wang, L.-C. A Simple Proof of Thue's Theorem on Circle Packing. *arXiv* **2010**, arXiv:1009.4322.
41. Tomašić, V. Application of the Monoliths in DeNOx Catalysis. *Catal. Today* **2007**, *119*, 106–113. [CrossRef]
42. Comsol. *CFD Module User's Guide*; Version 5.4; Comsol AB: Stockholm, Sweden, 2018. Available online: https://doc.comsol.com/5.4/doc/com.comsol.help.cfd/CFDModuleUsersGuide.pdf (accessed on 28 October 2023).
43. Comsol. *Chemical Reaction Engineering Module User's Guide*; Version 5.4; Comsol AB: Stockholm, Sweden, 2018. Available online: https://doc.comsol.com/5.4/doc/com.comsol.help.chem/ChemicalReactionEngineeringModuleUsersGuide.pdf (accessed on 28 October 2023).
44. Krocher, O.; Elsener, M. Combination of V_2O_5/WO^{3-} TiO_2, Fe^- ZSM_5, and Cu^- ZSM_5 Catalysts for the Selective Catalytic Reduction of Nitric Oxide with Ammonia. *Ind. Eng. Chem. Res.* **2008**, *47*, 8588–8593. [CrossRef]
45. Wilke, C.R. A Viscosity Equation for Gas Mixtures. *J. Chem. Phys.* **1950**, *18*, 517–519. [CrossRef]
46. Voglar, J.; Teržan, J.; Kroflič, A.; Huš, M.; Likozar, B. Mechanistic Modelling of Catalytic NOX Reduction Reactions after Hydrogen or Ammonia Combustion on Multiple Scales. *Renew. Sustain. Energy Rev.* **2023**, *186*, 113666. [CrossRef]
47. Cussler, E.L. *Diffusion: Mass Transfer in Fluid Systems*; Cambridge University Press: Cambridge, UK, 2009; ISBN 0521871212.
48. Liu, Z.; Yi, Y.; Zhang, S.; Zhu, T.; Zhu, J.; Wang, J. Selective Catalytic Reduction of NOx with NH3 over Mn-Ce Mixed Oxide Catalyst at Low Temperatures. *Catal. Today* **2013**, *216*, 76–81. [CrossRef]
49. Wang, Z.; Lan, J.; Haneda, M.; Liu, Z. Selective Catalytic Reduction of NOx with NH3 over a Novel Co-Ce-Ti Catalyst. *Catal. Today* **2021**, *376*, 222–228. [CrossRef]
50. Gonzo, E.E. Hydrogen from Methanol-Steam Reforming. Isothermal and Adiabatic Monolith Reactors' Simulation. *Int. J. Hydrogen Energy* **2008**, *33*, 3511–3516. [CrossRef]
51. Heiredal, M.L.; Jensen, A.D.; Thøgersen, J.R.; Frandsen, F.J.; Friemann, J. Pilot-scale Investigation and CFD Modeling of Particle Deposition in Low-dust Monolithic SCR DeNOx Catalysts. *AIChE J.* **2013**, *59*, 1919–1933. [CrossRef]
52. Cutler, A.H.; Antal Jr, M.J.; Jones Jr, M. A Critical Evaluation of the Plug-Flow Idealization of Tubular-Flow Reactor Data. *Ind. Eng. Chem. Res.* **1988**, *27*, 691–697. [CrossRef]
53. Moody, L.F. Friction Factors for Pipe Flow. *Trans. Am. Soc. Mech. Eng.* **1944**, *66*, 671–678. [CrossRef]
54. Gekas, I.; Vressner, A.; Johansen, K. *NOx Reduction Potential of V-SCR Catalyst in SCR/DOC/DPF Configuration Targeting Euro VI Limits from High Engine NOx Levels*; SAE Technical Paper 2009-01-0626; SAE International: Warrendale, PA, USA, 2009.
55. Cornejo, I.; Nikrityuk, P.; Hayes, R.E. The Influence of Channel Geometry on the Pressure Drop in Automotive Catalytic Converters: Model Development and Validation. *Chem. Eng. Sci.* **2020**, *212*, 115317. [CrossRef]
56. Lin, K.-S.; Mdlovu, N.V.; Juang, R.-S.; Tang, M.-T. Fine Structural Characterization of Noble Metals in Washcoat of Motorcycle Three-Way Converter Catalysts. *J. Environ. Chem. Eng.* **2023**, *11*, 109530. [CrossRef]